Methods to describe barotropic vortices by global fields and vortex characteristics

W.-G. Früh

Nonlinear Processes in Geophysics (2002) 9: 189–200

Nonlinear Processes in Geophysics

Methods to describe barotropic vortices by global fields and vortex characteristics

W.-G. Früh

Department of Mechanical and Chemical Engineering, Heriot-Watt University, Riccarton, Edinburgh, EH14 4AS, UK

Received: 1 August 2001 – Accepted: 17 October 2001

Abstract. Results from an experimental study of vortices in a rotating shear layer are presented. The data are in the form of maps of the instantaneous horizontal velocity field obtained by a particle tracking technique. Two fundamentally different methods to analyse time series of these velocity fields are presented and compared. One technique is the empirical orthogonal function (EOF) analysis, and the other method describes the flow field in terms of a few individual localised vortices.

The flows discussed here are time-dependent two-vortex flows, which could either be described as a global mode 2 or as a collection of four unequal vortices. The results show that, while EOF analysis is a very powerful tool to detect fairly regular travelling modes or stationary features, it cannot detect local dynamics. The vortex identification technique is very good at detecting local structures and events but cannot put them into the context of a global flow structure. The comparison of the techniques shows indications that the time-dependence found in the system for low mode numbers could arise from an interaction of the large scale, global-mode flow with a local mechanism of vortex generation and shedding at a solid boundary.

1 Introduction

The generation, evolution, and behaviour of coherent structures are fundamental problems in fluid mechanics. This paper will present data from an experimental study of vortex dynamics where the vortices originated from the instability of a detached shear layer within a rotating fluid. The mechanism and conditions for the instability of the shear layer, together with a detailed survey of flow regimes over a wide range of forcing parameters, were reported by Früh and Read (1999). Both, steady and time-dependent regular vortices were observed. One of the measurement techniques used was a particle tracking technique which resulted in sequences of horizontal velocity fields at regular time intervals. The aim of this paper is to present a description and comparison of two analysis techniques to describe the vortices most efficiently.

Correspondence to: W.-G. Früh (w.g.fruh@hw.ac.uk)

The remainder of this section is a short introduction to the background which is followed by a description of the experimental apparatus and the flow measuring technique. After a brief introduction to the general results, two alternative or complementary techniques will be presented. The first describes the flow in terms of individual vortices. After an initial analysis step in which the vortices are identified, the technique returns a typical vortex profile together with some scalars containing information about the position, size, and strength of the vortices. The second technique is the Empirical Orthogonal Function (EOF) analysis which decomposes the fields into empirical orthogonal functions (EOFs), each weighted by their respective variance contained in the singular values, λ, and principal components (PCs) which capture the time history of their associated EOFs. A variant in which the EOF analysis is applied to the fields rotated with the main flow feature, is also presented. While the standard EOF analysis does not require any pre-analysis, the variant EOF analysis and the vortex decomposition require a previous analysis step to identify the "*main flow feature(s)*".

1.1 Background

Rotating shear layers occur in a variety of situations, from industrial to geophysical applications. An example of an industrial application is the design of computer hard disk drives (Humphrey and Gor, 1993) where shear layers occur between the rapidly rotating magnetic disc and the stationary housing. It has been proposed that vortical features on the giant planets, such as the Great Red Spot on Jupiter, are a result of this instability (e.g. Meyers et al., 1989).

Compared to shear layers in non-rotating fluids, the effects of a background rotation are two-fold. For one, a strong Coriolis force inhibits motion aligned with the rotation axis and the flow tends to be two-dimensional and perpendicular to the rotation axis. The second effect is that a shear region, for

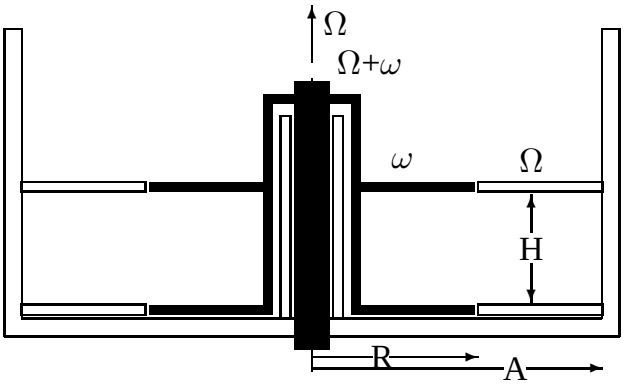

Fig. 1. Schematic diagram of the apparatus.

example due to an imposed velocity jump, is confined to a shear layer which becomes thinner as the background rotation becomes stronger. This scaling of the shear layer will obviously affect the shear instability of a fluid since the definition of the Reynolds number of the flow includes a length scale such as the shear layer thickness. The exact nature of the shear layer depends on the geometry of the domain and the forcing. In the simplest case of a uniform layer of fluid with horizontal boundaries and vertically uniform forcing of the shear flow, Stewartson (1957) has shown that the thickness of the shear layer is proportional to $\Omega^{-1/4}$, where Ω is the mean rotation. The apparatus was designed to investigate this basic case of a uniform layer of fluid with constant depth, horizontal boundaries, a vertical rotation axis, and uniform forcing. The first in-depth experimental studies of this system was carried out by Hide and Titman (1967), with a range of different realisations of such shear layers since then (Holton, 1971; Niino and Misawa, 1984; Antipov et al., 1986; Meyers et al., 1989; Solomon et al., 1993; Bergeron et al., 2000).

2 The apparatus

The fluid was contained in a cylindrical perspex tank with a radius of 300 mm as shown in Fig. 1. A vertical axis of radius 31.8 mm in the centre of the tank supported two circular disks with a radius of 150 mm each (the dark sections in Fig. 1. Two flat rings were placed in the tank flush with the circular sheets to ensure a uniform fluid depth throughout the domain. The height of the upper disk and ring above the lower surface could be adjusted from 30 to 150 mm but was kept at 100 mm for the experiments presented here. The working fluid in the particle tracking experiments was a water-glycerol mixture with a density of $\rho = 1044\,\mathrm{kg\,m^{-3}}$ and a kinematic viscosity of $\nu = 1.66 \times 10^{-6}\mathrm{m^2\,s^{-1}}$.

The inner axis with the disks was driven by a stepper motor at angular velocities ω ranging from -0.7 to $+0.7\,\mathrm{rad\,s^{-1}}$ ($\approx \pm 0.1\,\mathrm{Hz}$). The whole tank was mounted on a steel turntable with a diameter of 1.2 m which rotated anticlockwise at angular velocities up to $\Omega = 4\,\mathrm{rad\,s^{-1}}$ ($\approx 0.7\,\mathrm{Hz}$). The sign of the inner disk motion was taken as relative to the turntable rotation. The turntable rotation rate, Ω, and the inner disk rotation rate, ω, were controlled by a PC in such a way that any one of the dynamically relevant nondimensional parameters could be fixed while varying other parameters over time. The variation of a parameter could be any temporal function. In these experiments, a series of constant sections separated by linear changes was used.

2.1 Parameters

The main parameters in this system are the Ekman number and either the Rossby number or the Reynolds number. The Ekman number is a measure of the viscous dissipation compared to the Coriolis term,

$$E \equiv \frac{\nu}{\overline{\Omega} H^2} \tag{1}$$

where ν is the kinematic viscosity of the fluid, H the fluid depth. The mean rotation of the fluid, $\overline{\Omega}$, is often described in terms of the Coriolis parameter, $f = 2\overline{\Omega}$. The Rossby number,

$$Ro \equiv \frac{U}{fL} = \frac{1}{2}\frac{R}{L}\frac{\omega}{\overline{\Omega}}, \tag{2}$$

is a measure of the nonlinear advection compared to the Coriolis force, while the Reynolds number, Re, is a measure of the advection terms compared to viscous dissipation. The scaling velocity for Ro and Re is the velocity difference of the boundaries at the gap, $U = R\omega$. The definition of Re in this system varies from the usual definition, $Re = UL/\nu$, due to the fact that the length scale L is not a fixed scale relating to the apparatus but rather the shear layer thickness, which depends on the mean rotation rate as $L = (E/4)^{1/4} H$,

$$Re \equiv \frac{1}{\sqrt{2}} \left(\frac{\overline{\Omega} H^2}{\nu} \right)^{3/4} \frac{R}{H} \frac{\omega}{\overline{\Omega}}. \tag{3}$$

It may be noted here, that the Rossby and Reynolds numbers may be positive or negative. If the inner disk is rotating in the same sense as the turntable, Re is positive, and negative otherwise.

With a fluid depth of $H = 0.1\,\mathrm{m}$ and a kinematic viscosity of $\nu = 1.66 \times 10^{-6}\,\mathrm{m^2 s^{-1}}$, the typical ranges of these parameters were $|Re| \lesssim 3000$ and $E \approx 10^{-5} \ldots 10^{-2}$.

2.2 Particle Tracking experiments

During the Particle Tracking experiments, the horizontal velocity field in the horizontal plane at mid-level was measured. Pliolite particles suspended in the fluid were illuminated by a horizontal sheet of light which was produced by three projector light bulbs and cylindrical lenses arranged around the periphery of the tank. The horizontal flow field was then observed with a monochrome CCD camera looking vertically down on the tank. The camera was fixed to a superstructure on the turntable, and all velocity measurements were taken

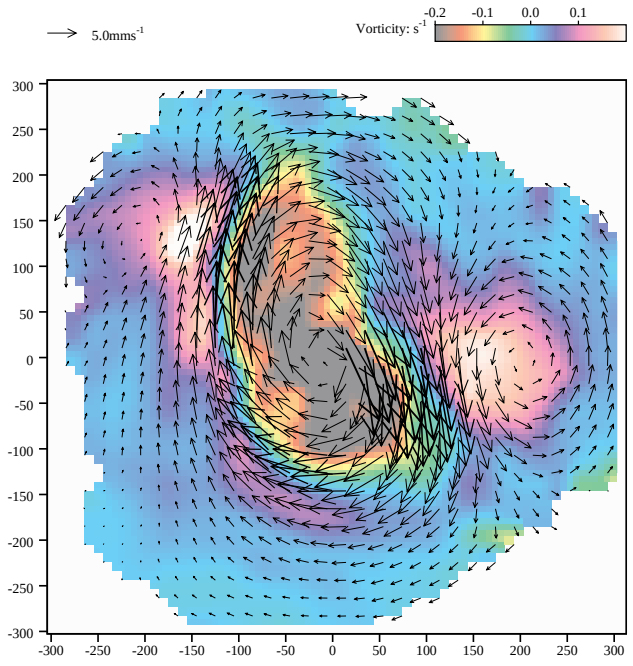

Fig. 2. Instantaneous velocity field and vorticity contour map of a distorted two-vortex flow at $Re = -80$ and $E = 7.3 \times 10^{-4}$.

relative to the tank. The size of the apparatus and the resolution of the camera required tracer particles with a diameter of 600 to 700 μm. Due to the slow velocities and the long observation periods, care had to be taken to adjust the density of the working fluid such that the particles were neutrally buoyant, which determined the fluid properties mentioned above.

To obtain a representative sample of flow states, three-hour periods were recorded onto S-VHS video tapes during which one of the parameters was changed. Two methods of changing the parameter were used, one where it was gradually increased or decreased linearly, the other where the parameter was changed linearly by a prescribed increment over a short time followed by a longer time where the parameters were held constant. For the analysis described in the following the piece-wise constant parameter setting was used.

The video tapes were then analysed using the particle tracking option of the flow measurement package **Dig***Image* (Dalziel, 1992), which resulted in a file of up to 4096 simultaneous horizontal velocity vectors at the position of identified tracer particles. While the software allowed a calculation of the velocities or derived quantities on a regular grid, the primary velocity data were used to minimize averaging and fitting errors.

3 Results

As presented in Früh and Read, 1999, the shear layer became unstable above a critical Reynolds number of $Re_c = 36 \pm 3$. The flow then broke up into a string of regular vortices where the size and number of vortices was mainly determined by the thickness of the layer as measured by the Ekman number. A small Ekman number resulted in a large number of small vortices while a large Ekman number resulted in as few as two vortices.

Increasing the Reynolds number gradually from the first supercritical vortex flow resulted in a successive transition to fewer and larger vortices along the shear layer. Reducing Re from a large value, produced a corresponding transition to more smaller vortices. The location of the transitions between different vortex numbers, however, depended on the direction of the change of the Reynolds number. This hysteresis resulted in the co-existence of up to three possible vortex states for any given pair of parameter values of E and Re. Which of the possible states was observed depended on the initial conditions but, once the flow had reached one of the states, it remained in that state for the duration of the experiment. The lowest number of vortices observed was two. All vortex flows with four or more vortices were steady wave-like flows with the appropriate symmetry of the wave number. Only flows with three or two vortices could show some time-dependence or deviations from rotational symmetry. This has also been observed in experiments in shallow-water experiments in rotating parabolic vessels by Bergeron et al. (2000) and numerical studies of those experiments by de Konijnenberg et al. (1999) where the time-dependent three-vortex flow was a spatial modulation of the basic three-vortex flow, and the time-dependent two-vortex flow occurred as a result of vortex generation and shedding at the inner boundary of the annular domain. In our experiments, the flow which would be described as a time-dependent three-vortex flow could have been an interference of modes two and three but conclusive evidence cannot be presented yet since the experiments gathering flow field data concentrated on the steady flows and the two-vortex flows. Two varieties of the two-vortex flow were found. One was a symmetric flow with two vortices of equal size and strength, equally spaced along the zonal direction. This flow was found after a mode transition $m = 3 \rightarrow 2$. The other two-vortex flow arose from a gradual distortion of the $m = 2$ flow into two vortices of unequal strength and shifted vortex positions. In a global mode description, this would be a superposition of a mode 1 and a mode 2. A pure mode 1 was never observed.

An example of a distorted two-vortex flow is shown in Fig. 2. The arrows represent the horizontal velocity field while the underlying contour map indicates the vorticity. The deformation of the shear region is clearly visible together with the two counter-rotating vortices along the outer edge of the shear layer. The light areas in the superimposed vorticity map indicate low-vorticity regions between the strongest shear and the centre of each vortex.

Removing the mean azimuthal flow from the velocity field in Fig. 2 results in pair of strong vortices next to each other in a dipole arrangement as shown in Fig. 3. The secondary vortex can still be seen, as well as another weak vortex pattern. The relative strength of the dipole and the weaker vortices varied not only for different experimental conditions, but it was also the main characteristic of time-dependent

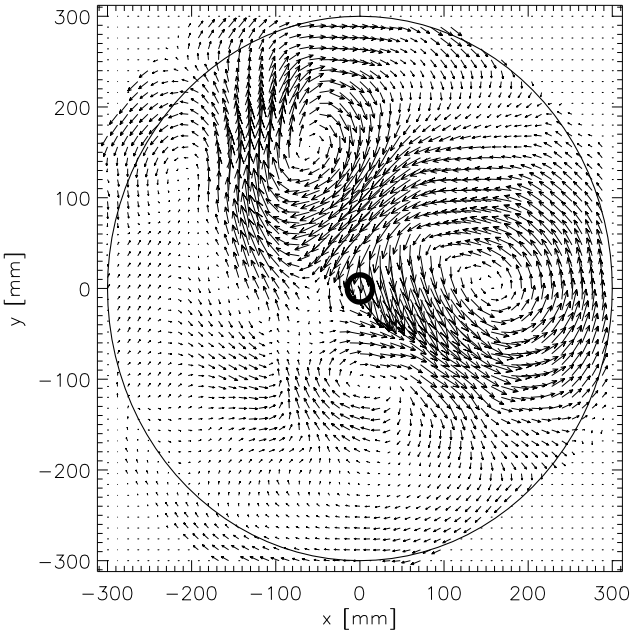

Fig. 3. Instantaneous eddy velocity field of the distorted two-vortex flow in Fig. 2.

behaviour. It was common to find that in any one flow field some of the vortices were almost circular while others showed pronounced eccentricity. The vortices tend to show less eccentricity at higher vortex numbers.

In the following section a sequence of velocity maps is analysed which starts in the distorted vortex regime and moves in steps towards lower Reynolds numbers and more symmetric two-vortex regime. After equilibration, the parameters are held constant for 12 min followed by a linear decrease of Re over 3 min, after which Re is held constant for 12 min once more, and so on. The Ekman number for these flows is $E = 7.3 \times 10^{-4}$, and the Reynolds numbers for the constant sections decrease from $Re = -167$ to -96 as listed in Table 1. To keep the amount of data at a manageable level, velocity fields were calculated at 30 s intervals.

4 Local vortex description

4.1 Isolation of vortices

As presented by Früh (2002), the main features of the flow field can be described as a superposition of a small number of coherent structures, or vortices. By normalising the variables and separating the radial and azimuthal variation of the scaled velocities, it is possible to find a generic, time-independent description of each vortex. The evolution is then expressed in time series of a small set of scalars and simple shape functions.

The flow was decomposed into four vortices, a primary and secondary cyclone and anticyclone each. While there were some differences between the four mean vortex fields,

Table 1. Physical and nondimensional parameters of experimental sequence used for analysis

R	= 150 mm	E	$= 7.3 \times 10^{-4}$
H	= 100 mm	$\overline{\Omega}$	= 0.22 rad/s
A	= 300 mm	ν	$= 1.66 \times 10^{-6}\mathrm{m}^2/\mathrm{s}$

Time (s)	0–720	900–1620	1800–2520	2700–3420
ω (rad/s)	–0.159	–0.136	–0.114	–0.0914
Ω (rad/s)	0.599	0.576	0.554	0.531
Ro	–0.7	–0.6	–0.5	–0.4
Re	–167	–143	–120	–96

they all showed an approximate velocity profile consistent with a

$$u_\xi \propto \xi \exp\left(-\xi^2\right) \tag{4}$$

behaviour where $\xi \in (0, 1)$ is the scaled radial coordinate from the vortex centre. The example shown in Fig. 4 is for the primary anticyclone.

4.2 Time series of vortex characteristics

The main scalars obtained from the decomposition into vortices are

- The coordinates of the vortex centre, either as (x, y) or (r, θ),
- The maximum radius of the vortex, R, and
- The maximum velocity in a vortex, V.

As discussed by Früh (2002), this is just a small selection of possible scalars, but these appear to show the most obvious temporal variation in the set analysed here.

Time series of the four scalars are shown in Fig. 5, where the position of the vortex is shown by their angle in the cylindrical system of the tank and their radial position as the distance of the core from the edge of the differentially rotating disks, $Y \equiv r - 150\,\mathrm{mm}$. The main features are that the four vortices drift on average at the same rate in a retrograde direction at a drift frequency of approximately $1.2 \times 10^{-2}\,\mathrm{rad\,s}^{-1}$, which is about 10% of the angular velocity of the inner disk, but that the drift of the individual vortices fluctuated, with very little fluctuation in the two primary vortices but pronounced fluctuation in the two secondary vortices. Similar variation is found in the radial position of the vortex centres, which seems to be locked to the angle. Due to the large difference in the amplitude of the variation in Y, we can conclude that this variation is not an artifact of the measuring system. It might still be a physical phenomenon caused by imperfections in the apparatus.

In the plots of the maximum radius ("size"), R, and the scaling velocity ("strength"), V, of the vortices it becomes apparent that the system gradually moves from one distinct dominant vortex to a state where the differences between the

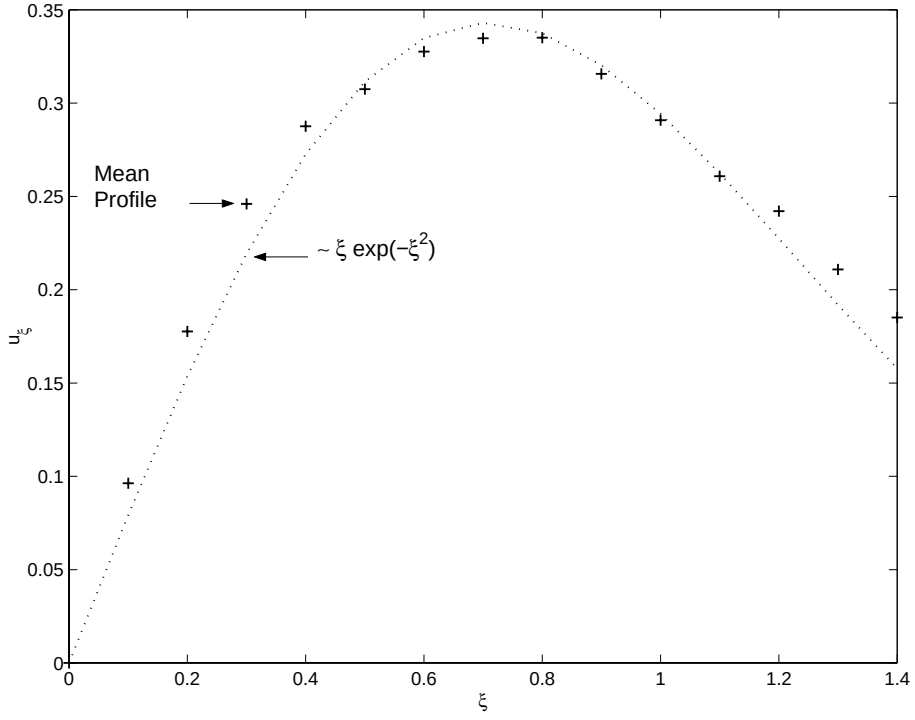

Fig. 4. Typical mean velocity profile. Superimposed is the function $0.8\xi \exp(-\xi^2)$.

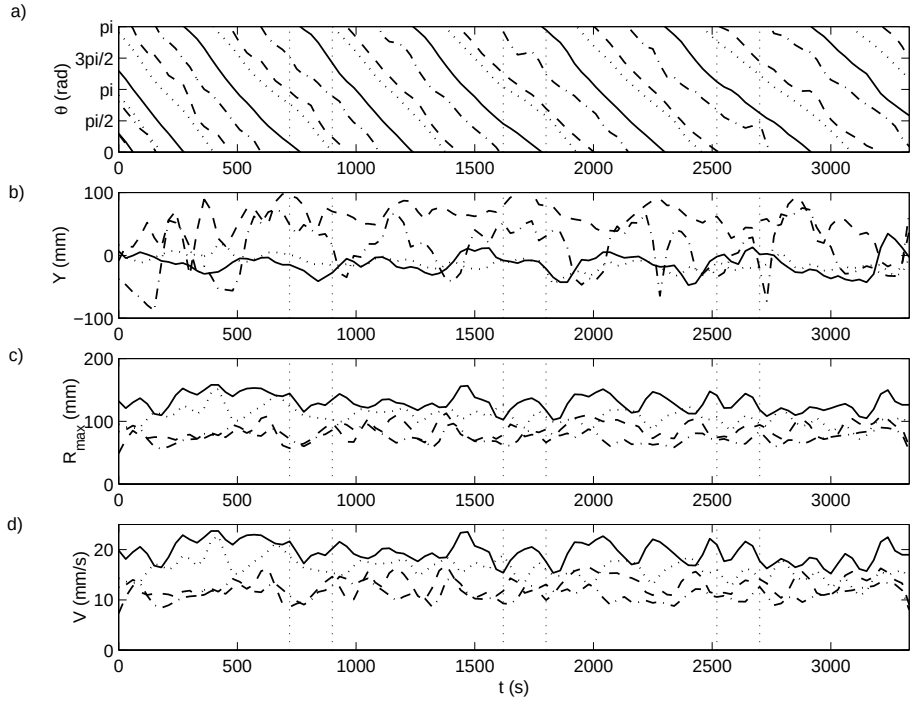

Fig. 5. Time series of the vortex characteristics: **(a)** Spatial phase of the vortex centres; **(b)** lateral distance of the vortex centre from the disk edge; **(c)** major radius of the vortices; and **(d)** maximum circulation velocity in the vortex. The solid line is for the primary anticyclone, the dotted line for the primary cyclone, the dashed line for the secondary anticyclone, and the dash-dotted line for the secondary cyclone.

two vortices of same sign gradually reduces. The average spatial extent of the individual vortices appears less affected than their strength as the forcing changes. One could conclude from this observation that the size of the vortices is primarily determined by the size of the tank and the total number of vortices present while the velocity scale depends

on the forcing by the inner disk rotation as well as the vortex size. As a result one might test the hypotheses that the vortex interactions are mainly controlled by the relative velocity scales, V, or by the relative vorticity scales, V/R. The time scales of fluctuations of R and V seem to be independent of the spatial phase of the vortices thus giving evidence of some "real" time-dependent behaviour due to vortex interactions, where the fluctuations of the two quantities are highly correlated with each other. Furthermore, the period of the fluctuations changes visibly as the forcing changes throughout the time series.

In summary, the decomposition into a set of vortices results in a mean vortex profile and time series of scalar vortex characteristics. It appears from the time series that the main temporal fluctuations are captured by the radial position and the vortex strength. While the dominant vortices move little from the zone of the shear forcing, the secondary vortices show large excursions relative to that zone. Other temporal behaviour is found in the vortex strength which appears to be linked with the mean vortex strength and the forcing. Using the mean profiles, one could develop some low-order models of this flow in terms of the position, size, and strength of the vortices, where the vortex interactions are primarily communicated by the relative vortex strengths.

5 Global field decomposition

5.1 Standard EOF analysis

Empirical Orthogonal Function (EOF) analysis, also known as Singular Systems Analysis (SSA) or Principal Component Analysis (PCA) is a standard statistical technique (e.g. Everitt and Dunn, 2001), which has been used extensively in many disciplines including Oceanography and Atmospheric Sciences (Brunet, 1994). It is based on the singular value decomposition of a suitable matrix of the ensemble of measurements. Numerically more reliable is the equivalent eigenvalue decomposition of the covariance matrix of the measurements. In the present case, each vector used to construct the measurement matrix contained the two horizontal velocity components interpolated onto a regular grid. In contrast to Particle Image Velocimetry (PIV) the raw data from particle tracking are not gridded, but depend on the actual location of identified particles.

Figure 6 shows the singular values for the EOF analysis of the full velocity field data sorted according to the relative contribution of each EOF to the observed variance between the velocity fields. The leading singular value is about three times larger than the second and third singular values which appear to form a pair. These are followed by two singular values of similar size and a 'shelf' before the values form a gradually decreasing tail. The tail indicates that a large number of EOFs represent noise of some form, presumably a combination of dynamical (red) noise and instrumental white noise. Pairing of two singular values frequently indicates a travelling mode which could be regarded as the empirical

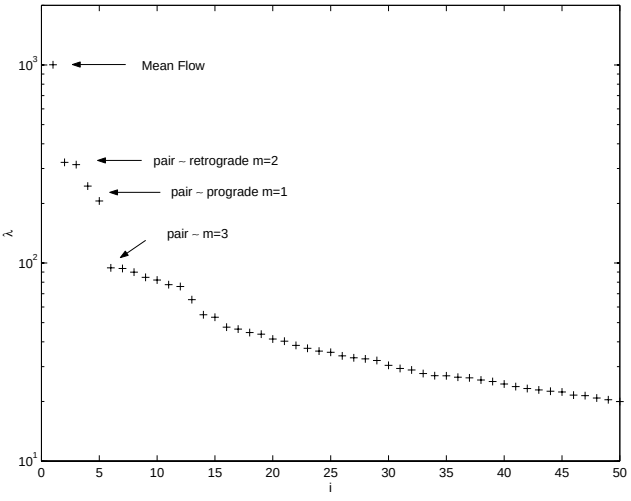

Fig. 6. Singular values for the EOF analysis of the set of full field data.

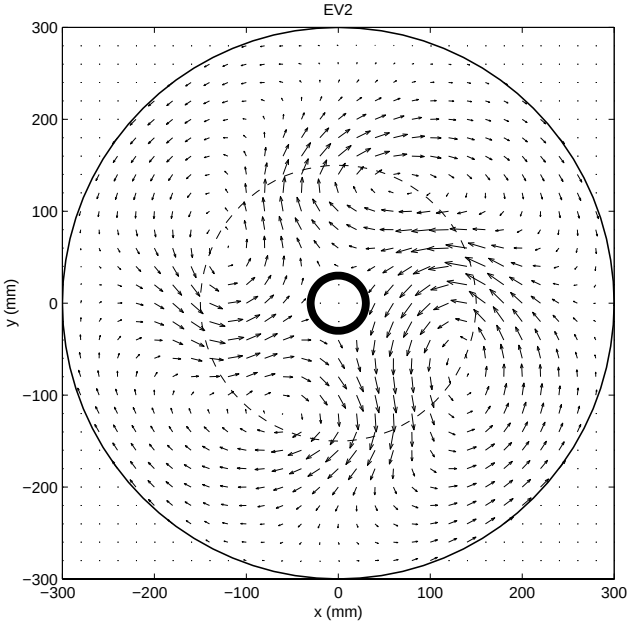

Fig. 7. Second EOF from the EOF analysis of the set of full field data.

equivalent of a sine and cosine mode of a Fourier expansion. As one might expect from this system in which a mean flow is forced by the inner disk which then results in drifting vortices, the EOF analysis yields a decomposition into the mean flow, a set of modes, and noisy fields, where the dominant mode is the azimuthal mean field. The other modes each consist of a pair of modes in quadrature, as is indicated by the pairing of singular values, e.g. λ_2 and λ_3, in Fig. 6. One has to keep in mind, however, that such pairing is only an indication and not firm evidence. The two EOFs corresponding to the first pair of singular values, EOF_2 and EOF_3, depict a mode 2 flow with two cyclonic and anticyclonic vortices

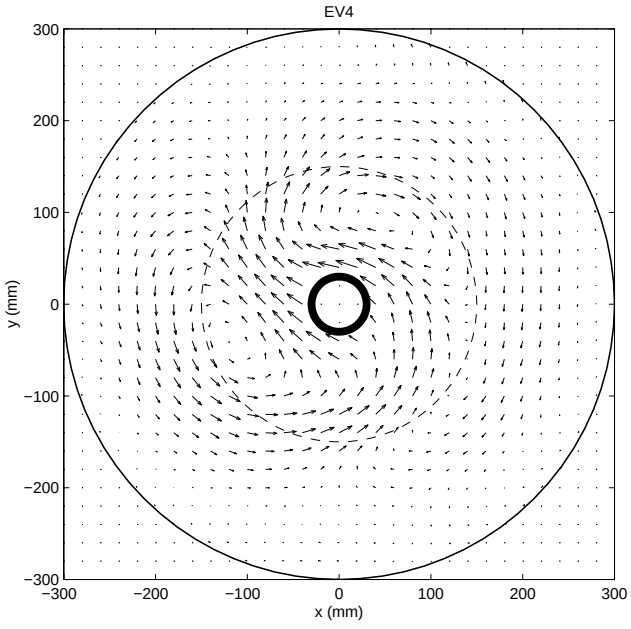

Fig. 8. Fourth EOF from the EOF analysis of the set of full field data.

each, evenly spaced around the tank as illustrated by EOF_2 in Fig. 7. The pair of EOFs following in the ranking are similar to a mode 1. As Fig. 8 shows, these EOFs are not equal to a harmonic mode 1 because the position of the centres of the cyclone and anticyclone are not evenly spaced but form an angle of about 53° with respect to the origin. The third pair of EOFs, almost indistinguishable from the noise-dominated tail, represents a mode 3. The mean flow and modes one and two contributed 44% to the total variance. While there is no clear signal-to-noise threshold, intuition allows to conclude that the flow is certainly dominated by the mean flow and two travelling wave modes. There may be further dynamically important modes just at the noise level, such as the mode 3, but any conclusion from this could not be supported as hard evidence.

The temporal evolution of the EOF contributions to the observed fields is captured by their corresponding principal components (PC). Since EOF_1 appears to represent the azimuthally averaged "mean flow" velocity field, the mean flow field at time t_i could be constructed as the product of the first Empirical Orthogonal Function (EOF_1), its corresponding first singular value (λ_1), and the i^{th} entry in the first Principal Component which corresponds to time t_i (PC_1^i):

$$\overline{\boldsymbol{u}}^j(t_i) = PC_1^i \; \lambda_1 \; \boldsymbol{EOF}_1{}^j,$$

where the superscript j is the index of the gridpoint. Since the grid had to be converted to vector for the decomposition, field j refers to a node in the two-dimensional grid with coordinates (x^j, y^j).

The solid line in Fig. 9a shows the first principal component vector, scaled by λ_1 as a time series. Since EOF_1 represents the azimuthal mean flow, the figure therefore shows the time series of the strength of the mean flow. The magnitude of that quantity is related to a velocity scale but it cannot be easily converted into standard units as the EOF analysis normalises its results. The mean flow in the sequence analysed here reveals some fluctuations around a mean value which decreases from 110 at $Re = -76$ to 80 at $Re = -96$. The following four PCs exhibit at first glance only a simple oscillation which reflects the drift of the mode in the frame of reference (not shown). It is more revealing to treat a pair of EOFs as modes and represent their behaviour in an amplitude, e.g. for mode 2,

$$A_2(t_i) = \left(\left(\lambda_2 PC_2^i\right)^2 + \left(\lambda_3 PC_3^i\right)^2 \right)^{1/2},$$

and a spatial phase with respect to the tank, e.g.

$$\phi_2(t_i) = \arctan\left(\frac{\lambda_3 PC_3^i}{\lambda_2 PC_2^i}\right).$$

The amplitude and phase for the first pair, PC_2 and PC_3, representing a mode 2, are shown as the dash-dotted line in Figs. 9a and b, respectively. The phase shows an almost steady retrograde drift (i.e. in the same sense as the forcing) at a mean angular drift velocity of $\omega_2 = -2.37 \times 10^{-2} \mathrm{rad\,s^{-1}}$ ($\approx 20\%$ of the inner disk's angular velocity), while the amplitude shows, besides a general trend with the change of the forcing, an oscillation in the strength of the mode 2 with an approximate period of $T \approx 500\,\mathrm{s}$, or an angular frequency of around $1.2 \times 10^{-2}\,\mathrm{rad\,s^{-1}}$. Since this frequency is half the drift frequency (within the current experimental uncertainties) it is possible that this oscillation could be either a real perturbation caused by imperfections in the apparatus, or even an artifact of the measuring system. The quantities for the second pair (the dotted lines in Figs. 9a and b, which represents a mode 1, show a prograde drift at $\omega_1 = 1.23 \times 10^{-2}$rad/s together with an oscillation of the amplitude similar to that of the mode 2 but in antiphase. The general trend is also present. The amplitude of the third pair ("mode 3") was much more erratic and, instead of a general drift, the phase vacillated around a constant value of $\phi_3 \sim \pi$ for $Re = -176$ and -143 and $\phi_3 \sim 0$ for the rest of the set. In terms of wave interactions, this phase relationship is consistent with a resonant triad between those modes, satisfying the resonance condition,

$$\sum \frac{\omega_m}{m} = \omega_2/2 + \omega_1 + \omega_3/3 = 0.$$

Comparing the drift frequencies of the modes with the drift frequency of the vortices as obtained from the direct identification of the vortices, as shown in Fig. figure 5, shows that the mode 2 drifts in the same direction as the vortices, but at twice the phase speed. However, its group velocity, $\omega_2/2$, is the same as the vortex drift frequency.

In summary, the standard EOF analysis confirms the initial impression obtained by pure inspection of the fields, namely that the flow is dominated on a large scale by a superposition of the mean flow and two travelling waves of wave numbers

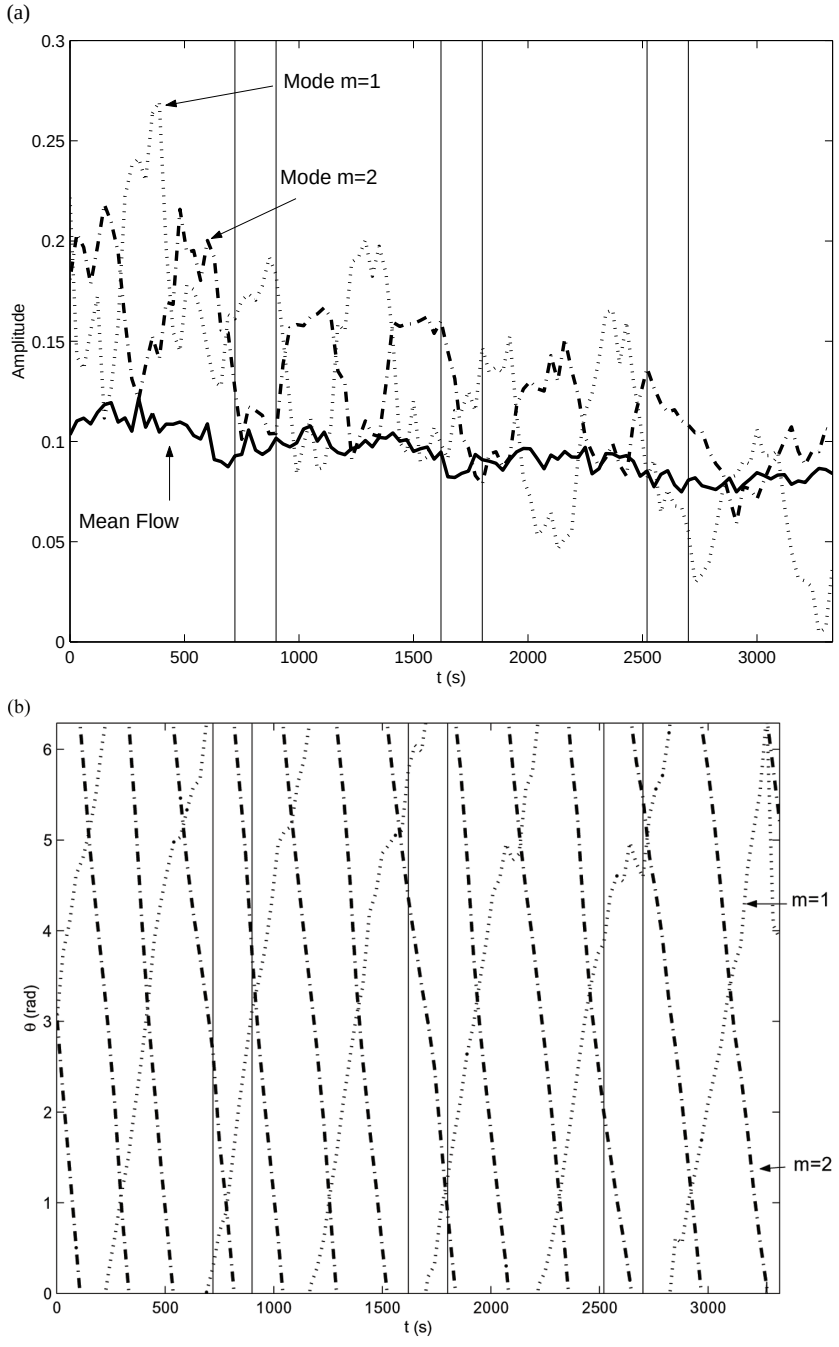

Fig. 9. Time series of the Principal Components from the EOF analysis of the set of full field data. All PCs are scaled with their singular value. **(a)** Amplitude of the first principal component (solid line) and "mode amplitudes" of the two successive pairs of principal components, PC_2 and PC_3 as the dash-dotted line, and PC_4 and PC_5 as the dotted line. **(b)** Phase of the pair PC_2 and PC_3 (dash-dotted line) and PC_4 and PC_5 (dotted line).

one and two. The principal component analysis shows that a time dependence initially observed as a vacillation between a strongly and a weakly distorted two-vortex flow can be described as a vacillation of the two modes in antiphase. In this framework of global modes, the two dominant modes travel in the opposite direction through the tank. Finally, one can observe in the relative contributions of modes one and two that the average distortion of the field at weaker forcing (smaller $|Re|$) is less than for stronger forcing.

5.2 EOF analysis of rotated eddy field

Several variants of the standard EOF analysis were tested to explore how information could be extracted in a more informative product. Removing the mean flow before applying the analysis returned results which were indistinguishable from

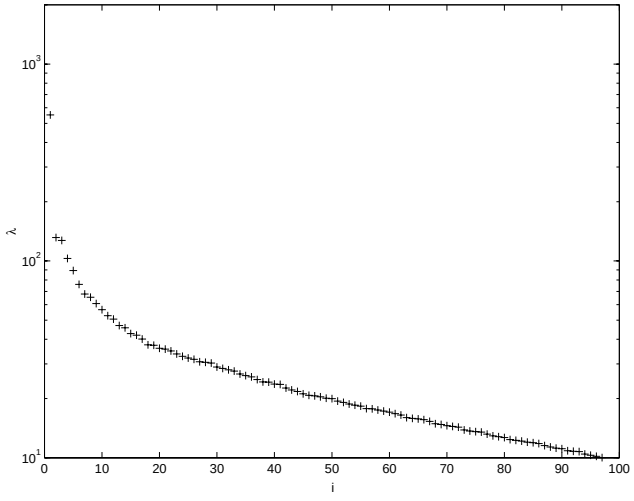

Fig. 10. Singular values for the EOF analysis of the set of rotated eddy fields.

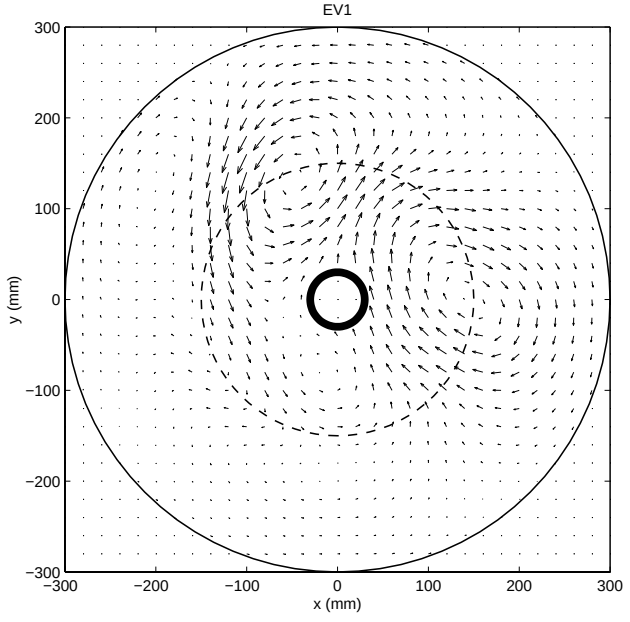

Fig. 11. First EOF from the EOF analysis of the set of rotated eddy fields.

the previous set with the exception that the mean flow was absent from the set of EOFs, i.e. the mode 2 was now described by the leading pair of EOFs, and so on.

Rotating the eddy field such that the phase of the dominant mode was subtracted simply changed the drift frequency of the modes, but not in a meaningful way. Instead one should better subtract $\phi_m(t)/m$, if m is the dominant wave number. In this section, however, we have used the angle of the main flow feature to rotate the coordinate system. This angle was obtained from the identification of the vortices described above in Sect. 4 and illustrated in Fig. 5a.

By using the eddy field only, the mean flow has been removed and does not show up in the EOFs. The singular value spectrum in Fig. 10 is dominated by a single singular value, although two more singular values seem to be paired. These three singular values contribute 24% to the total variance.

Due to the exploratory nature of EOF analysis, no statement can be made about their statistical significance. In this context, apparently irregular fluctuations of the corresponding PCs were taken as an indication that the structure in the respective EOF was noise-dominated and not "significant" in the description of the large-scale flow structures. Slow and distinct variability, on the other hand, was taken as an indication that it might be instructive to consider its corresponding EOF. Some extensions of EOF analysis include information about statistical significance, e.g. Allen and Smith (1994, 1997). The leading EOF, shown in Fig. 11, shows the two dominant vortices, now fixed in the rotating frame of reference. Two very weak vortices centred at $(-200, 100)$ and $(-50, -50)$, respectively, can just about be identified. This flow field is very similar to the instantaneous eddy field shown earlier in Fig. 3.

The second and third EOF are, despite the pairing in the singular values, not a pair of travelling waves. Instead, EOF_2, shown in Fig. 12, is dominated by a spatially extended but only moderately strong cyclonic feature located between the two dominant vortices in EOF_1 and a strong anticyclone located between the dominant cyclone and the weak anticyclone from EOF_1. In addition, a distinct cyclone is located in the lower half of the domain, centred at $(0, -150)$. This EOF_2 appears to be mainly a modulation of the main flow features with the same number of vortices but shifted around the tank. The third EOF, in Fig. 13, shows a different flow field, which is dominated by four vortices arranged in a single cyclone in the lower right quadrant and a tripolar structure in the upper left quadrant. The fact that the singular values, λ_2 and λ_3, are very similar gives rise to uncertainty as to how information is distributed among the two EOFs. The only constraints are that they are mutually orthogonal orthogonal and orthogonal to all other EOFs in the set. In principle, it would be possible to construct an infinite set of pairs of EOFs which all satisfy this condition but may appear to show very different spatial structures from those shown in Figs. 12 and 13.

Figure 14 shows time series of the first three principal components. The dotted line is PC_1 which is the amplitude of the dominant flow structure. This amplitude shows weak fluctuations and a non-zero mean which gradually reduces with the Reynolds number. The fluctuations do not show a clear periodicity but are in a well-defined range of periods of around 200 s to 250 s, which is between 4 and 5 times the inner disk's rotation period. This range of periods is in the same range as that of the retrograde drift of mode 2 in the standard EOF analysis as seen in Fig. 9. PC_2 and PC_3, the solid and dash-dotted lines respectively, show strong fluctuations which appear to be a superposition of a slow, large-amplitude oscillation and a weaker and faster oscillation. The faster oscillation is at a time scale of 100 s to 150 s, about half of the inner disk period, while the slow variations are on the order of 10 inner disk rotations.

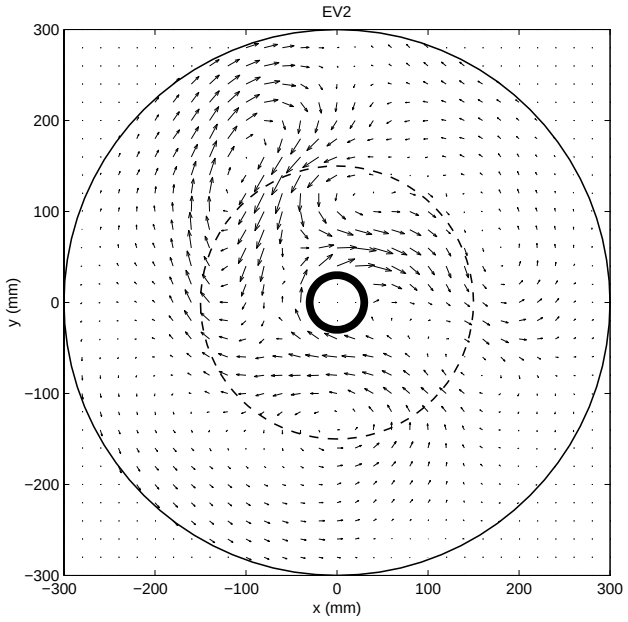

Fig. 12. Second EOF from the EOF analysis of the set of rotated eddy fields.

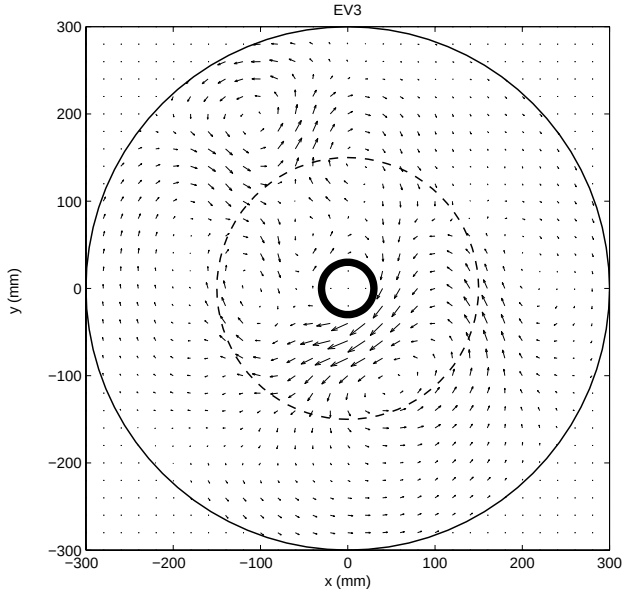

Fig. 13. Third EOF from the EOF analysis of the set of rotated eddy fields.

As the Reynolds number is decreased, PC_1 and PC_2 show a marked decrease (by about a factor of three) while PC_3 is less affected. The shift of the relative contributions of the separate EOFs to the flow field over the change of the forcing parameter captures a systematic drift in the flow structures. Since the shift is a gradual one, it appears that the change in the flow structures may be due to a supercritical bifurcation as opposed to a sudden mode transition. The oscillation of these two principal components appears to be mainly in phase towards the beginning of the total time series, and slightly shifted in the latter part of the time series. The absence of pairing of EOFs into travelling modes shows that the drift of the modes in opposite directions is an artifact of the rotation of the coordinate system with respect to the coherent structures. If the coordinate system rotates with the dominant coherent structure all other modulations of the field appear to be co-rotating with that structure. This can be compared with the Rössler-type attractor reconstructed for a single-point time series from a similar flow type in the experiment, as shown in Fig. 7 in Read and Früh (1999).

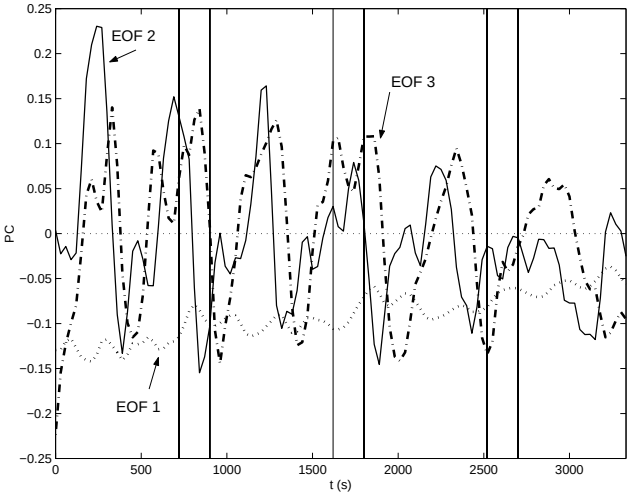

Fig. 14. Principal Components from the EOF analysis of the set of rotated eddy fields. All PCs are scaled by their singular values.

In summary, the rotated EOF analysis shows that all dynamics and gradual changes in dynamics, as the forcing changes, can be described by stationary flow structures. The dominant flow structure is clearly that of a dipole extending over just under half of the domain. The temporal fluctuations of the flow are best described by two stationary modulations, one of another mainly dipolar structure and one of a combination of a monopole and a tripole. It is likely that the modulation of the dominant dipole with the secondary dipole leads to a weakening of the overall dipole while the latter modulation then moves the flow field towards a more symmetric global wave-like structure of mode two.

6 Conclusions

Two methods for analysing sets or time series of velocity fields have been discussed. One method assumes that the fields can be characterised by global structures or modes and yields a set of empirical orthogonal eigenfunctions (EOFs) which characterise the full flow field together with their respective contribution. The standard version of the EOF analysis returned sets of travelling modes. The time series of the amplitudes and phases showed that the bifurcation following from the mode 2 flow was through a gradual increase of its spatial subharmonic, a mode 1, travelling at the same group velocity but in the opposite direction. The amplitudes

indicate that the mechanism is that of a mode competition since they were anticorrelated.

Rotating the frame of reference with the dominant flow feature did not result in a set of harmonic modes. Instead a large dipole emerged as the dominant feature, together with two stationary spatial modulations. The two modulation patterns worked in phase to effect a regular weakening of the dipolar structure and a corresponding strengthening of a mode 2 structure. The change of behaviour as a result of changing the forcing appeared to be related to a change in the relative weighting of the two modulation patterns.

A different approach regarded the vortices as separate but interacting localised coherent structures. The slow regular variations of the relative vortex locations corresponds directly to the mode competition observed in the framework of global structures. Additional fluctuations at shorter time scales, not resolved in the standard EOF analysis but also captured by the rotated EOF analysis, could also be identified in the strength and size of the vortices. The indications are that the strength of the vortices, as measured by their velocity scale, controls the dynamics of the flow and may be a cause of the observed fluctuations at both time scales.

Due to the vortex-wave ambiguity of the flows in the system, it appears to be most useful to use complementary techniques based in both frameworks, that of global modes and that of localised vortices, together. The standard EOF analysis as a technique, which requires little prior knowledge of the flow structures, is a powerful technique to extract dominant features but this strength comes at the price that it tends to seek sinusoidal normal mode patterns in a flow with drifting coherent structures. On the other hand, a description of the flow as individual features does not impose a global structure on the flow. This technique, however, requires considerable amounts of prior knowledge and processing. It is in the judgment of the user to choose the appropriate number of features in a flow field, and it is expected that the technique might be difficult to apply if structures appear and disappear at frequent intervals.

As an illustration of the relative merits, it is worth comparing our findings to discussions of time-dependent flows in the parabolic annular vessel with a differentially rotating split lower boundary of Bergeron et al. (2000). The authors observed that a modulation of a two-vortex flow arose from vortices generated at vortices at the inner core of the system, which then moved outwards to interact with the vortices centred near the split of the base. The standard EOF analysis would not be able to capture such a localised vorticity generation unless it always occurred at the same location. The technique would attempt to describe the variability by a superposition of other modes to the flow. The rotated EOF analysis would have similar difficulties, except that it would only reliably pick up vortex generation if it occurred at a fixed orientation to the dominant vortex. If the vortex generation were reproduced in the rotated EOF analysis, one could conclude that the generation arises from an interaction of the dominant vortex with the solid boundary. Finally, the vortex identification would easily pick up a new vortex. In the present implementation where a fixed number of vortices were chosen, the vortex tracking would might show a vacillation of the position of a chosen vortex. This is indeed observed in the lateral position of the secondary cyclone, which is the weaker structure of opposite vorticity compared to the strongest vortex. The longitudinal position, however, does not seem to show such a strong vacillation. From this discussion it appears that the flows discussed in this paper are equivalent to those observed in experiment and numerical simulation by Bergeron et al. (2000) and de Konijnenberg et al. (1999). While standard EOF gave a very clear answer about the global structures and the existence of time variability, it could not identify the origin and mechanism of the time-dependence. The rotated EOF might contain more information to the vortex generation at the inner shaft, but it is again somewhat obscured by the technique's attempt to find global modes. The structure of the second and third EOF, however, might contain the information in the form of radial modes where the beginning of a phase would locate a vortex near the shaft. The motion of that vortex would then be parameterised by a radial drift through part of a cycle until the vortex disappears into the structure of the first EOF. An indication to this representation might be seen in the slight shift in phase between the two principal components shown in Fig. 14. If further analysis of those EOFs supports this idea then this, together with the fact that the longitudinal position of the secondary cyclone in the vortex identification does not vacillate much, would support a mechanism of vortex generation in the frame of the drifting dominant vortices. In other words, vorticity is generated at the inner shaft by the flow of the dominant vortices.

To test and explore the vortex identification technique further it is recommended to apply it to other simple systems, such as vortex experiments in shallow layers or stratified fluids, and to results from numerical simulations of such fields. A prime candidate at present would be a numerical model of the detached shear layer in an annular gap by, e.g. Bergeron et al. (2000). A useful extension of the vortex identification would be to allow vortex generation and destruction, and vortex merging. Ultimately, one should explore its usefulness for field data, such as satellite data.

Acknowledgement. This research arose from a research project headed by P. Read and funded by the Natural Environment Research Council of the UK. I would like to thank P. Read for his constant support. I am grateful to R. Hide and the late D. Tritton for stimulating discussions and suggestions.

References

Allen, M. R. and Smith, L. A.: Investigating the origins and significance of low-frequency modes of climate variability, Geophys. Res. Lett., 21, 883–886, 1994.

Allen, M. R. and Smith, L. A.: Optimal filtering in singular systems analysis, Phys. Lett. A, 234, 419–428, 1997.

Antipov, S. V., Nezlin, M. V., Snezhkin, E. N., and Trubnikov, A. S.: Rossby autosoliton and stationary model of the Jovian Great Red Spot, Nature, 323, 238–240, 1986.

Bergeron, K., Coutsias, E. A., Lynov, J. P., and Nielsen, A. H.: Dynamical properties of forced shear layers in an annular geometry, J. Fluid Mech., 402, 255–289, 2000.

Brunet, G.: Empirical normal-mode analysis of atmospheric data, J. Atmos. Sci., 51, 932–952, 1994.

Dalziel, S. B.: Decay of rotating turbulence: some particle tracking experiments, J. Appl. Sci. Res., 49, 217–244, 1992.

de Konijnenberg, J. A. V., Nielsen, A. H., Rasmussen, J. J., and Stenum, B.: Shear-flow instability in a rotating fluid, J. Fluid Mech., 387, 177–204, 1999.

Everitt, B. and Dunn, G.: Applied Multivariate Data Analysis, Arnold, 2nd edn., 2001.

Früh, W.-G.: Extracting a general vortex profile for two-dimensional vortices in a rotating fluid, Phys. Fluids, submitted, 2002.

Früh, W.-G. and Read, P. L.: Experiments in a barotropic rotating shear layer. I: Instability and steady vortices, J. Fluid Mech., 383, 143–173, 1999.

Hide, R. and Titman, C. W.: Detached shear layers in a rotating fluid, J. Fluid Mech., 29, 39–60, 1967.

Holton, J. R.: An experimental study of forced barotropic Rossby waves, Geophys. Fluid Dyn., 2, 323–341, 1971.

Humphrey, J. A. C. and Gor, D.: Experimental observations of an unsteady detached shear layer in enclosed corotating disk flow, Phys. Fluids, A 5, 2438–2442, 1993.

Meyers, S. D., Sommeria, J., and Swinney, H. L.: Laboratory study of the dynamics of Jovian-type vortices, Physica D, 37, 515–530, 1989.

Niino, H. and Misawa, N.: An experimental and theoretical study of barotropic instability, J. Atmos. Sci., 41, 1992–2011, 1984.

Read, P. L. and Früh, W.-G.: Flow-field and point velocity measurements in a barotropically unstable shear layer, Phys. Chem. Earth (B), 24, 461–466, 1999.

Solomon, T. H., Holloway, W. J., and Swinney, H. L.: Shear flow instabilities and Rossby waves in barotropic flow in a rotating annulus, Phys. Fluids A, 5, 1971–1982, 1993.

Stewartson, K.: On almost rigid rotations, J. Fluid Mech., 3, 17–26, 1957.